Atmospheric Environment 216 (2019) 116922

Contents lists available at ScienceDirect

Atmospheric Environment

journal homepage: www.elsevier.com/locate/atmosenv

On the nature of sea salt aerosol at a coastal megacity: Insights from Manila, Philippines in Southeast Asia

Mojtaba AzadiAghdam[a], Rachel A. Braun[a], Eva-Lou Edwards[a], Paola Angela Bañaga[b,c], Melliza Templonuevo Cruz[b,d], Grace Betito[c], Maria Obiminda Cambaliza[b,c], Hossein Dadashazar[a], Genevieve Rose Lorenzo[b], Lin Ma[a], Alexander B. MacDonald[a], Phu Nguyen[e], James Bernard Simpas[b,c], Connor Stahl[a], Armin Sorooshian[a,f,*]

[a] Department of Chemical and Environmental Engineering, University of Arizona, Tucson, AZ, USA
[b] Manila Observatory, Quezon City, 1101, Philippines
[c] Department of Physics, School of Science and Engineering, Ateneo de Manila University, Quezon City, 1108, Philippines
[d] Institute of Environmental Science and Meteorology, University of the Philippines, Diliman, Quezon City, 1101, Philippines
[e] Department of Civil and Environmental Engineering, University of California-Irvine, Irvine, CA, USA
[f] Department of Hydrology and Atmospheric Sciences, University of Arizona, Tucson, AZ, USA

A B S T R A C T

This study utilizes multiple aerosol datasets collected in Metro Manila, Philippines to investigate sea salt aerosol characteristics. This coastal megacity allows for an examination of the impacts of precipitation and mixing of different air masses on sea salt properties, including overall concentration and size-resolved composition, hygroscopicity, and morphology. Intensive size-resolved measurements with a Micro-Orifice Uniform Deposit Impactor (MOUDI) between July–December 2018 revealed the following major results: (i) sea salt levels exhibit wide variability during the wet season, driven primarily by precipitation scavenging; (ii) ssNa$^+$ and Cl$^-$ peaked in concentration between 1.8 and 5.6 μm, with Cl$^-$ depletion varying between 21.3 and 90.7%; (iii) mixing of marine and anthropogenic air masses yielded complex non-spherical shapes with species attached to the outer edges and Na$^+$ uniformly distributed across particles unlike Cl$^-$; (iv) there was significant contamination of sea salt aerosol by a variety of crustal and anthropogenic pollutants (Fe, Al, Ba, Mn, Pb, NO_3^-, V, Zn, NH_4^+); (v) categorization of samples in five different pollutant type categories (Background, Clean, Fire, Continental Pollution, Highest Rain) revealed significant differences in overall Cl$^-$ depletion with enhanced depletion in the submicrometer range versus the supermicrometer range; (vi) κ values ranged from 0.02 to 0.31 with a bimodal profile across all stages, with the highest value coincident with the highest sea salt volume fraction in the 3.2–5.6 μm stage, which is far lower than pure sea salt due to the significant influence of organics and black carbon. Analysis of longer term $PM_{2.5}$ (particulate matter with aerodynamic diameter less than 2.5 μm) and PM_{coarse} (= PM_{10} – $PM_{2.5}$) data between August 2005 and October 2007 confirmed findings from the MOUDI data that more Cl$^-$ depletion occurred both in the wet season versus the dry season and on weekdays versus weekend days. This study demonstrates the importance of accounting for two factors in future studies on sea salt: (i) non-sea salt (nss) sources of Na$^+$ impact calculations such as for Cl$^-$ depletion that typically assume that total Na$^+$ concentration is derived from salt; and (ii) considering precipitation data over a larger spatial domain rather than a point measurement at the study site to investigate wet scavenging.

1. Introduction

As one of the most abundant aerosol types globally on a mass basis (Liao et al., 2006), sea salt has far-reaching impacts on the planet including scattering of light, geochemical cycling of nutrients, exchanging moisture with the atmosphere, and serving as cloud condensation nuclei (CCN) to impact clouds and the water cycle (Lewis and Schwartz, 2004). Sea salt is also significant with regard to halogen chemistry in the atmosphere as the reactions of acids with sea salt particles can lead to emissions of reactive iodine, bromine, and chlorine (Chameides and Stelson, 1992). Sea salt is estimated to account for ~30% of global aerosol optical depth (Bellouin et al., 2013), with most studies investigating its behavior near the surface or within the boundary layer owing to such low levels in the upper troposphere, which is far-removed from its sources at the surface (Murphy et al., 2019). Sea salt's strong vertical gradient qualifies this aerosol type as especially important for studying wet scavenging processes, which is an area requiring improvement in atmospheric models (MacDonald et al., 2018; Murphy et al., 2019).

Two important aspects of atmospheric sea salt requiring further research are the nature of its mixing with other pollutant types and its sensitivity to precipitation. Southeast Asia is a prime candidate region for the study of these two topics due to extensive precipitation during parts of the year (e.g., Southwest Monsoon (SWM) season), extensive

* Corresponding author. Department of Chemical and Environmental Engineering, University of Arizona, PO BOX 210011, Tucson, AZ, 85721, USA..
E-mail address: armin@email.arizona.edu (A. Sorooshian).

https://doi.org/10.1016/j.atmosenv.2019.116922
Received 15 June 2019; Received in revised form 21 August 2019; Accepted 24 August 2019
Available online 28 August 2019
1352-2310/ © 2019 Elsevier Ltd. All rights reserved.

issues with air pollution, and numerous growing coastal megacities in the region. One such coastal megacity is Metro Manila, Philippines, with a population of 12.88 million (Philippine Statistics Authority, 2015). This urban area is impacted by long-range transport from other countries in Southeast and East Asia and has significant local emissions (e.g., vehicular traffic, industrial activity, burning, waste processing, smelting). Studying aerosol properties when these non-marine air masses mix with sea salt is important owing to poorly understood chemical changes in particles upon such mixing. For example, there can be depletion of particulate species (e.g., Fe, Cl) when marine air mixes with plumes from ships and wildfires (Braun et al., 2017; Sorooshian et al., 2013) while methanesulfonate (MSA) levels tend to be higher when fire plumes mix with marine air as compared to either air mass type alone (Sorooshian et al., 2015).

The goal of this work is to report on size-resolved properties of aerosol during an intensive period of measurements between July–December 2018, in addition to a longer-term dataset (August 2005–October 2007) of $PM_{2.5}$ (particulate matter with aerodynamic diameter less than 2.5 μm) and PM_{10} composition. The following questions will be addressed: (i) how does the concentration of sea salt vary as a function of particle size and what are size-resolved morphological traits of these particles?; (ii) how do sea salt concentrations differ across different temporal scales and as a function of meteorological parameters such as precipitation accumulation?; (iii) how does chloride depletion depend on particle size and what species are most responsible?; (iv) what are the size-resolved hygroscopic properties of sea salt-containing particles?; and (v) what is the general impact of sea salt mixing with other pollutant types? The implications of the subsequently discussed results extend to improved understanding of sea salt properties, their chemical reactivity, and the role of wet scavenging in modifying surface layer PM concentrations in urban regions. These findings are relevant for modeling, remote sensing applications, and for contrasting with other regions to determine how reproducible our results are in other areas.

2. Materials and methods

2.1. Study site description

Measurement data used in this study were collected in Quezon City, Philippines at the Manila Observatory (MO; 14.64° N, 121.08° E) (Fig. 1). The site represents a coastal megacity with influence from long-range transport of pollution, marine emissions, and a variety of regional urban sources such as vehicular emissions, industrial activity, waste processing, and burning (Cohen et al., 2009). The study includes data from two different periods, including a longer-term characterization of $PM_{2.5}$ and PM_{10} between 14 August 2005–23 October 2007 and a more intensive period of size-resolved PM measurements between 19 July 2018–7 December 2018. The latter period is associated with the year-long study referred to as the Cloud, Aerosol, and Monsoon Processes Philippines Experiment ($CAMP^2Ex$) weatHEr and CompoSition Monitoring (CHECSM) study. For the purposes of subsequent discussion, data are divided between wet (June–October) and dry (November–May) seasons based on the degree of influence from monsoonal precipitation. While there can be variability in the onset and end of these periods (Bagtasa et al., 2018; Cruz et al., 2013), it is important to note that there was a statistically significant difference in the mean values of precipitation accumulation between dry and wet seasons based on the intensive measurements summarized in Table 1 (p value = 0.02 using two sample *t*-test).

2.2. Size-resolved aerosol measurements: July–December 2018

2.2.1. Sample collection and extraction

Between 19 July and 7 December 2018, 21 sets of samples (Table 1) were collected by two separate Micro-Orifice Uniform Deposit Impactors (MOUDI, MSP Corporation) (Marple et al., 2014) on the 3rd floor of the MO office building (~85 m above sea level). These measurements cover the SWM season (MO1 – MO16) and then, beginning with set MO17, the transition into the dry season that typically begins in November. The MOUDIs collected aerosol particles on substrates with the following aerodynamic cutpoint diameters (D_p): 18, 10, 5.6, 3.2, 1.8, 1.0, 0.56, 0.32, 0.18, 0.10, 0.056 μm. For the 21 MOUDI sets, Teflon substrates (PTFE membrane, 2 μm pore, 46.2 mm, Whatman) were used. There were two special instances when two MOUDI sets were simultaneously collected with the two individual MOUDI instruments for the purpose of conducting different types of analyses (i.e., chemical analysis versus gravimetric analysis) on the separate sets of substrates. One additional MOUDI set collected on 1 August 2018 (11:53–13:00 local time; not shown in Table 1) involved aluminum substrates for the purpose of microscopy analysis.

With the exception of MOUDI sets MO3 and MO13, Teflon substrates were cut in half with one half stored in a freezer and the other half placed in a sealed polypropylene vial with 8 mL of 18.2 MΩ-cm Milli-Q water and sonicated for 30 min.

2.2.2. Sample analyses

The resulting aqueous extracts were chemically analyzed with ion chromatography (IC; Thermo Scientific Dionex ICS - 2100 system) for water-soluble ions and triple quadrupole inductively coupled plasma mass spectrometry (ICP-QQQ; Agilent 8800 Series) for water-soluble elements. Instrument details for the IC were as follows: columns = AS11-HC 2 × 250 mm (Anion) and CS12A 2 × 250 mm (Cation); suppressors = AERS 500e 2 mm (Anion; 28 mA) and CERS 500e 2 mm (Cation; 22 mA); Eluents = KOH (Anion) and MSA (Cation); flow rate = 0.4 ml min^{-1}; chromatographic methods: 5 min equilibration, 2–8 mM from 0 to 20 min, 8–28 mM from 20 to 30 min (Anion) and 5 min equilibration, 5 mM from 0 to 13 min, 5–18 mM from 13 to 16 min, 18 mM from 16 to 30 min (Cation). The IC species discussed in this work include Na^+, NH_4^+, Mg^{2+}, Ca^{2+}, amines (the sum of dimethylamine, diethylamine, and trimethylamine), MSA, pyruvate, adipate, succinate, maleate, oxalate, phthalate, Cl^-, NO_3^-, and SO_4^{2-}. For ICP, all of the reagents and tuning solutions were procured from Agilent. Samples were acidified using 2% nitric acid before analysis. The ICP species discussed here include K, Al, Fe, Mn, Ti, Ba, Zn, Cu, V, Ni, P, Cr, Co, As, Se, Rb, Sr, Y, Zr, Nb, Mo, Ag, Cd, Sn, Cs, Hf, Tl, and Pb.

References in this study to total water-soluble mass refer to the concentration sum of the aforementioned IC and ICP species. Table S1 reports the limit of detection (LOD) of these species as calculated with the method of Miller and Miller (2000). Sets MO3 and MO13 underwent gravimetric analysis with a Sartorius ME5-F microbalance. Details related to the LODs associated with these measurements are reported by Cruz et al. (2019) for the same dataset. Blank samples were processed the same way as the measurement samples, with blank concentrations subtracted from sample concentrations.

Aluminum substrates from the one collected microscopy set were analyzed for morphology and elemental composition with a Hitachi S-4800 High Resolution Scanning Electron Microscopy (SEM) equipped with a Thermo Noran system Six Energy Dispersive X-ray Spectrometer (EDX) in the Kuiper Imaging Cores Facility at the University of Arizona. For SEM-EDX analysis, a small section was cut from the center of substrates and taped on a sample stub with double-sided carbon tape. Samples were analyzed under vacuum without sputtering coating. During analysis, particles were randomly selected and examined by 30 eV acceleration voltage and 100–125 μA probe current under high magnification mode. EDX data were obtained after SEM analysis for determining chemical composition of individual particles. As a blank substrate contains Al (~91.5%), C (~5.4%), Ag (~2.1%), and O (~0.9%), these elements cannot be evaluated for quantitative purposes.

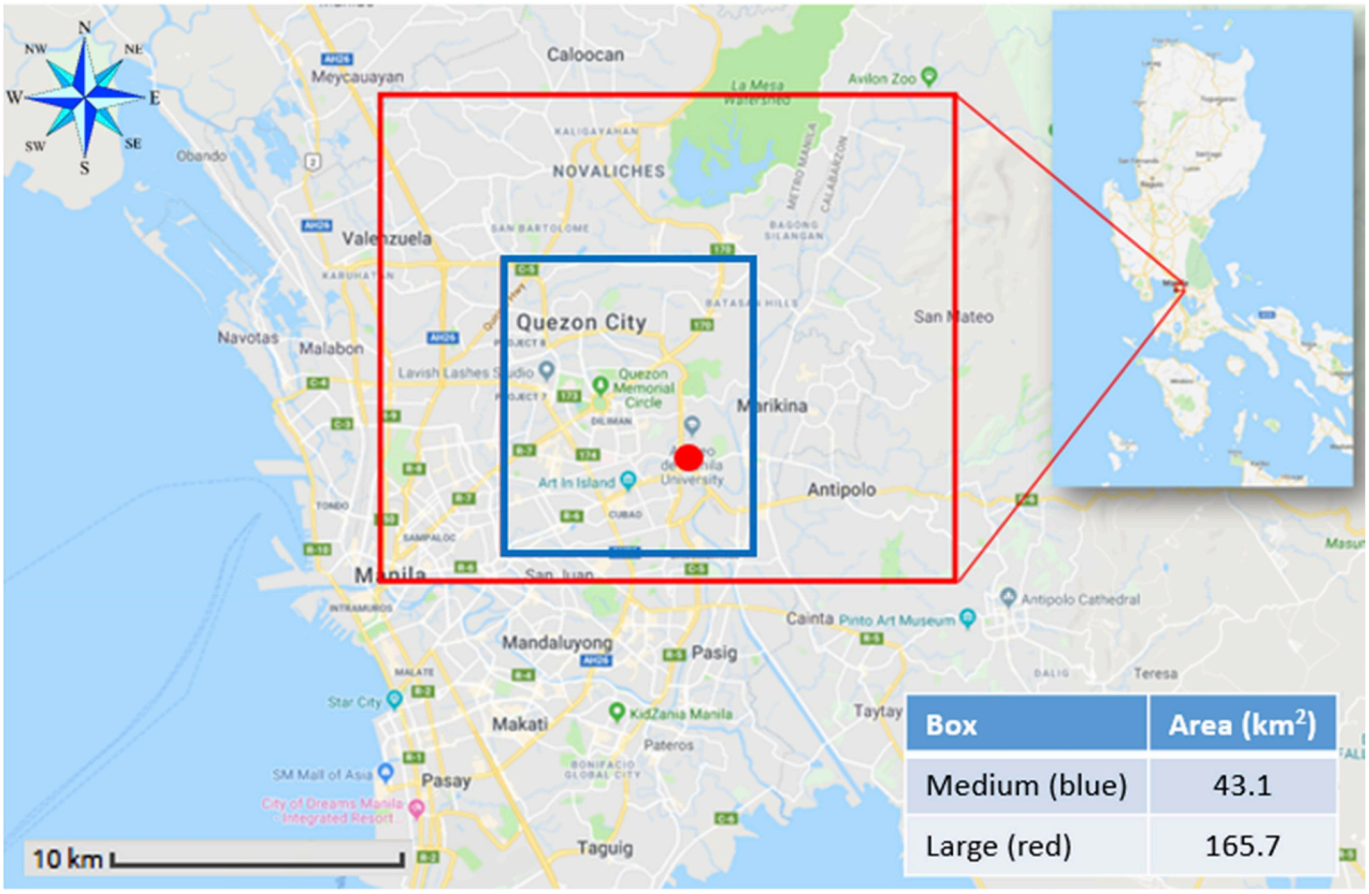

Fig. 1. Location of the sample station at the Manila Observatory (MO) marked with red circle in Metro Manila, Philippines, with an additional inset map showing a wider region of the Philippines. The two rectangles represent different spatial domains over which precipitation data were obtained for comparison to the aerosol data collected at MO. (For interpretation of the references to color in this figure legend, the reader is referred to the Web version of this article.)

2.3. $PM_{2.5}$ and PM_{coarse} measurements: August 2005–October 2007

To complement the shorter term MOUDI data, longer term data (14 August 2005–23 October 2007) are analyzed here to understand temporally relevant characteristics over the course of an annual cycle. These measurements were collected at 3 m above ground level at MO. Two Airmetrics Minivol samplers were used to simultaneously collect $PM_{2.5}$ and PM_{10} samples using 47 mm diameter ringed Teflon substrates and an Andersen Dichotomous sampler was used to collect another pair of $PM_{2.5}$ and PM_{coarse} (i.e., PM_{10}-$PM_{2.5}$) samples using 37 mm diameter ringed Teflon substrates. Samplers were programmed to run for 24 h periods beginning at midnight. Substrate samples were individually extracted in 25 ml of 18.2 MΩ-cm Milli-Q water via sonication for 1 h. A Dionex ICS-1000 ion chromatography system was then used for

Table 1
Summary of MOUDI sample set details and associated meteorological conditions, total resolved water-soluble mass concentrations, and sum of $ssNa^+$ and Cl^-.

Sample set name	Sampling dates	Duration (h)	Flow rate (L min^{-1})	Wind speed (m s^{-1})	Wind direction (°)	T (°C)	Rain (mm)	Water-soluble mass (μg m^{-3})	$ssNa^+$ + Cl^- (μg m^{-3})
MO1	Jul 19–20	24	30	3.3	90.1	24.9	29.1	4.6	0.6
MO2	Jul 23–25	54	30	1.3	95.8	26.7	13.1	6.5	1.0
MO3/4	Jul 25–30	119	29/30	1.2	111.8	26.7	16.1	5.2	0.6
MO5	Jul 30-Aug 1	42	29	2.6	98.1	27.5	15.3	9.2	1.1
MO6	Aug 6–8	48	27	0.9	127.5	26.1	40.2	5.1	0.5
MO7	Aug 14–16	48	28	3.0	107.8	27.8	3.3	13.7	2.6
MO8	Aug 22–24	48	29	3.5	108.7	28.1	12.2	12.8	1.5
MO9	Sep 1–3	48	27	0.7	98.6	26.6	44.8	6.2	0.2
MO10	Sep 10–12	48	29	1.0	94.7	26.2	34.1	6.4	0.2
MO11	Sep 18–20	48	27	0.5	290.2	27.8	31.2	2.7	0.4
MO12	Sep 26–28	48	27	1.2	96.3	27.8	4.3	13.5	2.2
MO13/14	Oct 6–8	48	30/26	0.6	108.2	27.8	1.6	16.6	0.6
MO15	Oct 15–17	48	30	0.4	157.7	27	30.5	5.1	0.1
MO16	Oct 23–25	48	29	0.7	229.2	28.1	0	7.2	0.6
MO17	Nov 6–8	48	30	1.3	71.4	27.7	0.1	4.9	1.5
MO18	Nov 10–12	48	29	1.2	68	27.5	0	6.1	1.65
MO19	Nov 19–21	48	31	1.5	30.7	27.4	20.4	4.5	0.9
MO20	Nov 27–29	48	30	1.1	44.3	27.2	0	5.9	1.1
MO21	Dec 5–7	48	31	1.2	94.4	27.8	0	4.3	1.7

speciation and quantification of the following ions: F^-, Cl^-, NO_2^-, Br^-, NO_3^-, PO_4^{3-}, SO_4^{2-}, Li^+, Na^+, NH_4^+, K^+, Mg^{2+}, Ca^{2+}.

2.4. Meteorological data

Meteorological data were collected using a Davis Vantage Pro 2 Plus weather station co-located with the aerosol measurements at MO. Rain amounts were extracted from the Precipitation Estimation from Remotely Sensed Information using Artificial Neural Networks—Cloud Classification System (PERSIANN-CCS) dataset, which is available from the University of California Irvine Center for Hydrometeorology and Remote Sensing (CHRS) Data Portal (http://chrsdata.eng.uci.edu) (Nguyen et al., 2019). The PERSIANN-CCS algorithm extracts local and regional cloud features (coldness, geometry, texture) from infrared geostationary satellite imagery for estimating rainfall at 0.04° × 0.04° spatial resolution every 30 min. More details about PERSIANN-CCS can be found in Hong et al. (2004). Nguyen et al. (2014) showed that PERSIANN-CCS successfully captured heavy rainfall of Typhoon Haiyan over the Philippines in November 2013. In order to study the impact of spatial domain of rain data on aerosol concentrations, data were collected over three spatial domains (Fig. 1): point location at MO = 14.64° N, 121.08° E; medium box = 14.61°–14.69° N, 121.02°–121.10° E; large box = 14.60°–14.74° N, 120.98°–121.16° E. Unless otherwise noted, references to rain accumulation are in reference to the latter large box.

2.5. Transport modeling

In order to assess the impacts of synoptic and regional scale transport on sea salt concentration at MO, 96 h back-trajectories were obtained from the Hybrid Single-Particle Lagrangian Integrated Trajectory (HYSPLIT) model (Rolph et al., 2017; Stein et al., 2015) ending 500 m above ground level at the MO (14.64° N, 121.08° E) sampling site. For each sampling period, trajectories were obtained every 6 h using the National Centers for Environmental Prediction/National Center for Atmospheric Research (NCEP/NCAR) reanalysis data with the "Model vertical velocity" method.

2.6. k-Köhler theory

One of the goals of this study was to quantify relative differences in hygroscopicity as a function of particle diameter with a focus on MOUDI stages most enhanced with sea salt. A common way to quantify hygroscopicity is with the single parameter kappa, κ (Petters and Kreidenweis, 2007). For multicomponent aerosol, an overall κ for each stage of individual MOUDI sets is calculated using a mixing rule approach. More specifically, the Zdanovskii, Stokes, and Robinson (ZSR) method (Stokes and Robinson, 1966; Zdanovskii, 1948) assists in finding κ by weighing each species' κ_i by its volume fraction, ε_i:

$$\kappa = \sum_i \varepsilon_i \kappa_i \tag{1}$$

In the present study, the water-soluble components were measured as individual ions. However, since κ values are documented for compounds, not ions, in the literature, the measured ions needed to be allotted into their original compounds. This was done using an established ion pairing scheme (Gysel et al., 2007), which uses individual species concentrations to derive compound concentrations. In addition to the water-soluble fraction, water-insoluble organics and black carbon (BC) contribute significantly to ambient PM. For set MO13, total mass, BC mass, and water-soluble concentrations were known (Cruz et al., 2019); note that BC was measured with a Multi-wavelength Absorption Black Carbon Instrument (MABI; Australian Nuclear Science and Technology Organisation), which is an optically-based technique from which data were used based on absorption at 870 nm (Cruz et al., 2019) The remaining mass was attributed to water-insoluble organics. In order to derive a κ more representative of ambient PM, probable concentrations of water-insoluble organics and BC were applied to all other MOUDI sets using the relative fractions of these two components found in set MO13. Although such scaling is not fully accurate across all the MOUDI sets, it provides some sense of more realistic values with the assumption that both the relative amount of emissions of all aerosol species (and precursors) and the rates of formation and removal were stable throughout the study period. As noted by Cruz et al. (2019), the qualitative trend in BC concentration across the MOUDI stages was consistent for all sets collected. For inclusion into Equation (1), values of density and κ were adopted from the literature for each pure compound, including water-insoluble organics and BC (Table S2).

2.7. Calculations related to sea salt

While in marine environments aerosol Na^+ and Cl^- are typically attributed to marine emissions due to their abundance in sea salt (ss), there can be non-sea salt (nss) contributions to these species as well. Separation of the ss and nss contributions is especially important for Manila as it is impacted by diverse continental and marine emission sources. Examples of sources other than sea salt for Na^+ include biomass burning (Hudson et al., 2004; Silva et al., 1999), dust (Farren et al., 2019) and biological particles (China et al., 2018), the latter of which accounted for ~69% of total Na^+ mass during the wet season in the Amazon basin. Other sources of Cl^- include biomass burning, fossil fuel combustion, industrial activity, and crustal matter (Artaxo et al., 1994; Sorooshian et al., 2011; Wonaschutz et al., 2011; Ye et al., 2003). Airborne measurements by Lee et al. (2003) off the east coast of Asia near the present study region revealed that Cl^- was likely associated with crustal material aloft. Measurements in Shanghai, China suggested that the Cl^- depleted from salt particles can re-enter the aerosol phase via reactions with bases such as ammonia to form smaller salts (Ye et al., 2003).

Following ideas motivated by others (Becagli et al., 2005; Boreddy and Kawamura, 2015; Farren et al., 2019), we simultaneously solved Equations (2)–(5) to obtain $ssNa^+$, $nssNa^+$, $ssCa^{2+}$, and $nssCa^{2+}$ concentrations based on the average Ca^{2+}:Na^+ ratios (on a mass basis) in crustal matter and sea water being 1.78 and 0.038, respectively (Becagli et al., 2005; Boreddy and Kawamura, 2015; Bowen, 1979; Farren et al., 2019). This method allows for a more accurate estimate of nss SO_4^{2-} concentration using $ssNa^+$ in Equation (6) with knowledge that the mass ratio of SO_4^{2-}:Na^+ in sea water is 0.253 (Becagli et al., 2005; Boreddy and Kawamura, 2015; Farren et al., 2019). Excess (Ex) SO_4^{2-} is quantified using Equation (7), which is the remaining nss SO_4^{2-} after accounting for the amount forming a salt with NH_4^+ (Braun et al., 2017), with the latter portion referred to as "Neutralized SO_4^{2-}".

$$ssNa^+ = Na^+ - nssNa^+ \tag{2}$$

$$nssCa^{2+} = nssNa^+ \times \left(\frac{Ca^{2+}}{Na^+}\right)_{crust} \tag{3}$$

$$nssCa^{2+} = Ca^{2+} - ssCa^{2+} \tag{4}$$

$$ssCa^{2+} = ssNa^+ \times \left(\frac{Ca^{2+}}{Na^+}\right)_{sea\ water} \tag{5}$$

$$nssSO_4^{2-} = SO_4^{2-} - 0.253 \times ssNa^+ \tag{6}$$

$$Ex\ SO_4^{2-} = nss\ SO_4^{2-} - \left(\frac{MW_{sulfate}}{MW_{ammonium}}\right) \times \frac{NH_4^+}{2} \tag{7}$$

Using MOUDI data, Fig. 2 illustrates the impact of using this new approach (referred to as 'New method') to quantify the fraction of Na^+ associated with sea salt as compared to attributing all of the measured Na^+ to sea salt ('Old method'). The ranges of mass concentrations for $ssNa^+$ and $nssNa^+$ using the "New method" were 0–0.51 μg m^{-3} and 0–0.09 μg m^{-3}, respectively, with the average ratio of $ssNa^+$ to total

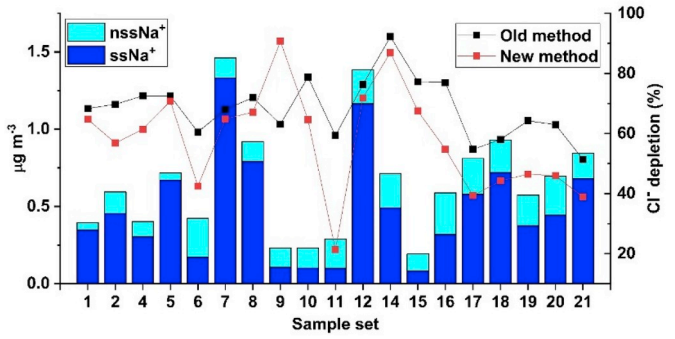

Fig. 2. MOUDI set averages of both $nssNa^+$ and $ssNa^+$, as calculated using Equations (2)–(5). On the right y-axis are $\%Cl^-$ depletion values based on using total Na^+ ('Old method') and $ssNa^+$ ('New method').

Na^+ being 0.63 ± 0.36 with minimum and maximum values of 0 and 1, respectively. Therefore, there is a non-negligible difference that has an impact on other calculations, such as those described below.

According to Fig. 2, Sets MO9-11 exhibited similar total Na^+ concentrations with exactly the same $ssNa^+$ concentration. While using the 'Old method' would result in categorizing these sets as background due to mid-range % Cl^- depletion, the 'New method' results reveal a wide difference in % Cl^- depletion such that the lowest and highest % Cl^- depletion happens in these sets. Possible reasons for the significant difference in Cl^- depletion for these sets with similar total Na^+ concentrations is discussed later.

Marine aerosols often have a lower Cl^-:$ssNa^+$ ratio compared to sea water, which is typically attributed to the release of gaseous Cl to the atmosphere (Martens et al., 1973). An important aspect of this work is quantification of Cl^- depletion owing to reactions of sea salt particles with inorganic and organic acids, leading to the release of gaseous Cl from the aerosol phase. The following equation is used to compute depletion based on the mass ratio of Cl^-:$ssNa^+$ in pure sea water being 1.81 (Martens et al., 1973; Zhao and Gao, 2008):

$$\%\ Cl^- \text{ depletion} = \frac{(1.81 \times ssNa^+ - Cl^-)}{(1.81 \times ssNa^+)} \times 100\% \quad (8)$$

In instances of the Cl^-:$ssNa^+$ ratio exceeding 1.81, $\%Cl^-$ depletion was considered to be 0% as in other work (Braun et al., 2017). For the MOUDI data analysis, set-averaged $\%Cl^-$ depletion values reported in this work represent the average of values for individual stages, excluding the first two and last two stages (i.e., 0.056, 0.1, 10, 18 μm) owing to very low $ssNa^+$ or Cl^- mass concentrations that can result in extreme ratios. Also, if the $ssNa^+$ value for a given stage was zero, that stage was not considered for calculations of $\%Cl^-$ depletion, with the presumption that any Cl^- from that stage stemmed from sources other than sea salt. As Cl^- also has nss sources, values of $\%Cl^-$ depletion discussed subsequently represent a lower bound and thus a conservative value for the degree of sea salt reactivity.

For the longer-term $PM_{2.5}$ and PM_{10} measurements (Section 2.3), data points with $ssNa^+$ values equal to 0 were similarly excluded from $\%Cl^-$ depletion calculations. Furthermore, data points with Cl^- concentrations exceeding a whole set's average plus two times its standard deviation for the entire dataset were also excluded due to the assumption that such samples are biased by nss sources.

The following equation was used to quantify the theoretical maximum amount of Cl^- depletion attributable to specific species (Braun et al., 2017; Song et al., 2018):

$$\%Cl^- \text{depletion due to X} = X \times y \times \frac{\left(\frac{MW_{Cl^-}}{MW_X}\right)}{(1.81 \times ssNa^+ - Cl^-)} \times 100\% \quad (9)$$

where X is the mass concentration of the acidic species of interest and y signifies the charge of the fully deprotonated conjugate base of X.

Lastly, calculations related to the degree of aging and contamination of sea salt particles were conducted using the following equation for mass-based enrichment factor (EF):

$$\text{Enrichment factor for X} = \frac{\left(\frac{X}{ssNa^+}\right)_{sample}}{\left(\frac{X}{ssNa^+}\right)_{control}} \quad (10)$$

where X is the species of interest, and $ssNa^+$ is the reference species. Control values used for the denominator were calculated based on the composition of pure sea water (Seinfeld and Pandis, 2006); for elements with a range of concentrations reported in sea water, the upper bound was used for X in the denominator of Equation (10).

3. Results and discussion

3.1. Relationships between sea salt and meteorology

The MOUDI sampling period between 19 July and 7 December 2018 was characterized by widely ranging mass concentrations of sea salt (0.1–2.6 μg m^{-3}), quantified here as the sum of $ssNa^+$ and Cl^- for all stages of each MOUDI set (i.e., $D_p \geq 0.056$ μm) (Table 1 and Fig. 2). When comparing the MO sets collected in the wet season (July–October; MO1-16) versus subsequent dryer months (November–December; MO17-21), the meteorological parameters in Table 1 exhibiting the largest differences were (wet/dry) rain (19.7 ± 15.1/4.1 ± 9.1 mm) and wind direction (130 ± 59/62 ± 25°), with less variability in wind speed (1.49 ± 1.10/1.26 ± 0.15 m s^{-1}) and temperature (27.1 ± 0.9/27.5 ± 0.2 °C). There were four MOUDI sets for which no rain was recorded (MO16, 18, 20, 21). The highest rain accumulation recorded was 44.8 mm for set MO9 (1–3 September). Interestingly, total water-soluble mass was more enhanced in the wet season than the dry season (8.20 ± 4.24 versus 5.14 ± 0.82 μg m^{-3}, respectively). In contrast, sea salt showed the opposite behavior (wet season = 0.87 ± 0.75 versus dry season = 1.37 ± 0.35 μg m^{-3}), presumably due to factors such as sensitivity of sea salt to wet scavenging (i.e., more removal in wet season). This is further supported by rain accumulation (large box in Fig. 1) being less strongly correlated to the overall sum of water-soluble mass ($r = -0.40$) as compared to both sea salt mass ($r = -0.69$) and $ssCa^{2+}$ ($r = -0.72$) (Table S3).

For the three spatial domains in Fig. 1 over which precipitation data were collected (point site at MO, medium box, large box), there was a significant negative relationship between rain accumulation and sea salt (scatterplots in Fig. S1), with the correlation coefficient becoming more negative as the domain size grew (MO: $r = -0.51$, $p = 0.03$; medium box: $r = -0.64$, $p < 0.01$; large box: $r = -0.69$, $p < 0.01$). Fig. S1 also shows r^2 values for a linear fit over the three domains. While r^2 values are not very strong, they show an increasing trend from MO (0.26) to the large box (0.48). One plausible explanation for the change is that transported PM is impacted by wet scavenging and thus precipitation impacts should be investigated over larger domains rather than with point measurements that are co-located with aerosol monitoring instrumentation. Future work is ongoing to more robustly address the relationship between aerosol mass and precipitation in the study region with a more extensive dataset covering a full year.

Relationships between sea salt and winds were varied as shown graphically with wind and pollution rose plots in Fig. 3. During the study period, winds at the sampling site were usually from the east or east-southeast, which are the directions coincident with the highest wind speeds and the highest and second highest concentrations of $ssCa^{2+}$ and sea salt. Wind speed exhibited a moderate positive correlation with sea salt ($r = 0.47$, $p = 0.04$) and $ssCa^{2+}$ ($r = 0.49$, $p = 0.04$) (Table S3), which is consistent with what others have observed in different regions (van Pinxteren et al., 2015). Conversely, wind direction had a moderate negative correlation with sea salt ($r = -0.32$, $p = 0.18$) and $ssCa^{2+}$ ($r = -0.35$, $p = 0.15$), suggesting

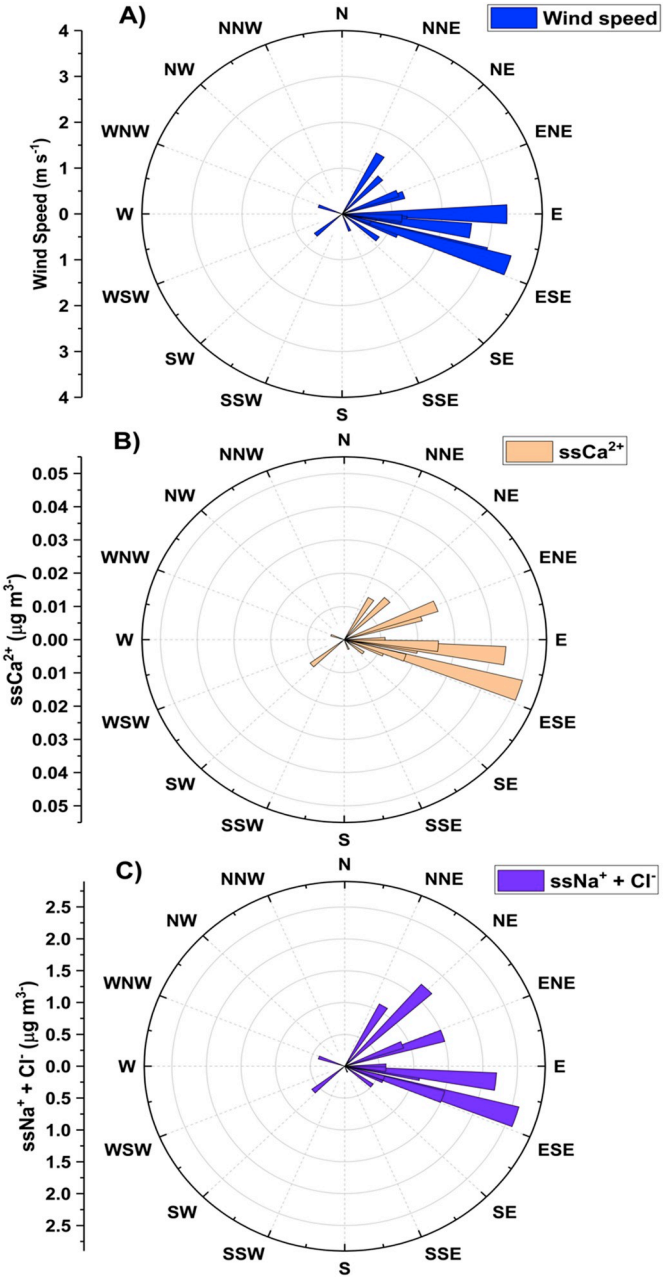

Fig. 3. Rose plots for A) wind speed, B) $ssCa^{2+}$, and C) sea salt mass.

that local terrain did not lead to significant variability in sea salt levels at MO. Note that there are mountains to the east unlike the bay area to the west.

To gain a broader view of air mass transport patterns impacting sea salt, Fig. 4 shows 96-h back-trajectories colored by $ssNa^+$ and Cl^-. The trajectories followed a southwesterly flow in the SWM months (July–October), which then transitioned towards northeasterly flow as is typical usually starting in November and extending through the boreal winter months (Bagtasa et al., 2018). Altitudes along most back-trajectories were contained within the bottom 1 km but did reach as high as 3 km. The results indicate no preferred direction among the two prevailing trajectory patterns with regard to higher or lower sea salt concentrations. This can be explained by the fact that the source of sea salt surrounds Manila as it is on an island and precipitation (the main sink) extends all around the region.

3.2. Speciated mass size distributions

Fig. 5A reveals that Na^+ and Cl^- were most concentrated in the supermicrometer diameter range with a predominant peak usually between 1.8 and 5.6 µm; distributions for individual sets are shown in Fig. S2. Similar results of sea salt peaking in the supermicrometer diameter range have been demonstrated in a host of other regions such as the Iberian Peninsula, western Europe, the Mediterranean (Quinn et al., 2000), the western coast of the United States (Maudlin et al., 2015; McInnes et al., 1994) and near the Arctic Ocean (Kerminen et al., 1998). Fig. 5B shows the mean mass size distributions of the select aerosol-phase acids that can chemically react with sea salt leading to Cl^- depletion. Two of the potential depleting agents (nss SO_4^{2-} and organic acids) exhibited most of their mass in the submicrometer range and peaked between 0.32 and 0.56 µm, while NO_3^- was most concentrated in the supermicrometer range peaking between 1.8 and 3.2 µm.

The $\%Cl^-$ depletion was significant for the entire sampling period with values ranging between 21.3 and 90.7% and a mean value of 57.9% (Fig. 2). Although not very large, there was a difference in mean $\%Cl^-$ depletion values between the wet season (61.9 ± 35.3%) and dry season (47.1 ± 37.4%). The higher mean depletion in the wet season can potentially be linked to the combination of a higher combined amount of the acids (NO_3^-, Ex SO_4^{2-}, organic acids) participating in Cl^- depletion (wet = 1.21 ± 0.64 µg m^{-3}, dry = 1.10 ± 0.68 µg m^{-3}) and lower $ssNa^+$ (wet = 0.46 ± 0.39 µg m^{-3}, dry = 0.56 ± 0.13 µg m^{-3}).

The mass size distribution of Na^+ was unique for set MO9 with a peak in the submicrometer size range (Fig. 5). Characteristics of set MO9 included having one of the lowest sample-averaged wind speeds (0.7 m s^{-1}) and the single highest rain amount (44.8 mm). The combination of a low wind speed and especially high rain (and thus wet scavenging potential) is consistent with factors expected for low ambient sea salt concentrations. Set MO6 exhibited slight higher wind speed (0.9 m s^{-1}) and lower rain amount (40.2 mm), but did not have the peculiar mass size distribution behavior as MO9, which warrants a deeper look into the relative importance of different factors that lead to the preferential removal of Na^+ in the supermicrometer mode with larger datasets.

3.3. Sea salt reactivity

An advantage of the longer duration of the bulk PM measurements as compared to the available MOUDI data was the ability to further examine Cl^- depletion effects between the wet and dry seasons using more data, and to also compare weekday (Mon-Fri) and weekend (Sat-Sun) periods (Fig. 6). The Cl^-:$ssNa^+$ mass ratio was lower for $PM_{2.5}$ as compared to PM_{coarse}, regardless of it being the wet (0.32 ± 0.48 vs 1.46 ± 0.46) versus dry (0.59 ± 0.60 vs 1.59 ± 0.43) season, or weekend (0.55 ± 0.54 vs 1.57 ± 0.42) versus weekday (0.43 ± 0.55 vs 1.48 ± 0.47). This is presumably due to the higher concentration of acids relative to Cl^- in $PM_{2.5}$ as compared to PM_{coarse}. While organic acid data were unavailable for the long-term bulk PM data, the mass size distributions from MOUDI measurements (Fig. 5) reveal that organic acids are generally more enhanced for $PM_{2.5}$ (similar to SO_4^{2-}) as compared to PM_{coarse}. Nitrate was enhanced in PM_{coarse} relative to $PM_{2.5}$, and thus NO_3^- was likely most actively involved with depletion in the coarser sea salt-containing particles.

Enhanced Cl^- depletion in the wet season versus the dry season was likely driven by higher Ex SO_4^{2-} and NO_3^- concentrations in the wet season, although, as will be shown subsequently using MOUDI data, organic acids may also play a large role. The higher Cl^- depletion during weekdays can be explained by more anthropogenic activity yielding more acids in the ambient aerosol, which is more evident for $PM_{2.5}$ due to almost twice as much Ex SO_4^{2-} compared to weekends.

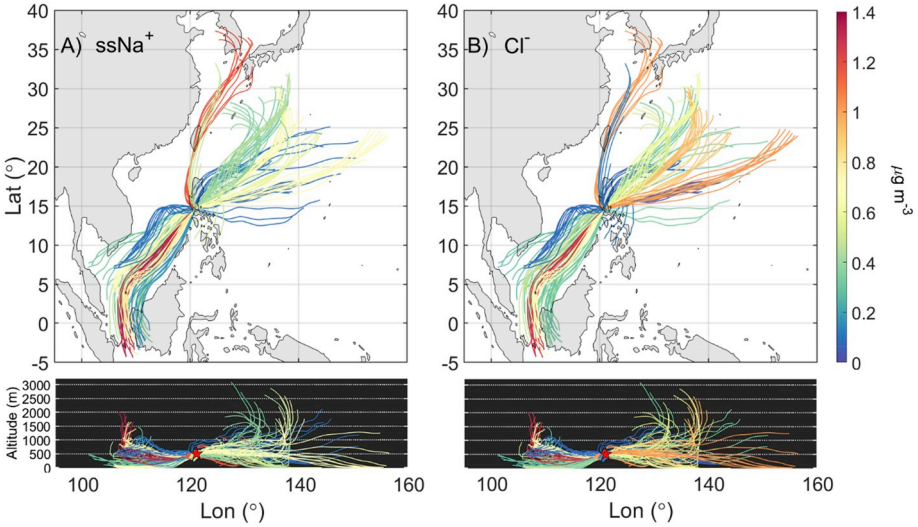

Fig. 4. Air mass back-trajectories associated with MOUDI sample sets that are colored by their A) $ssNa^+$ and B) Cl^- concentrations at the sample site in Metro Manila. The bottom panels represent altitudes of air masses along the back-trajectories.

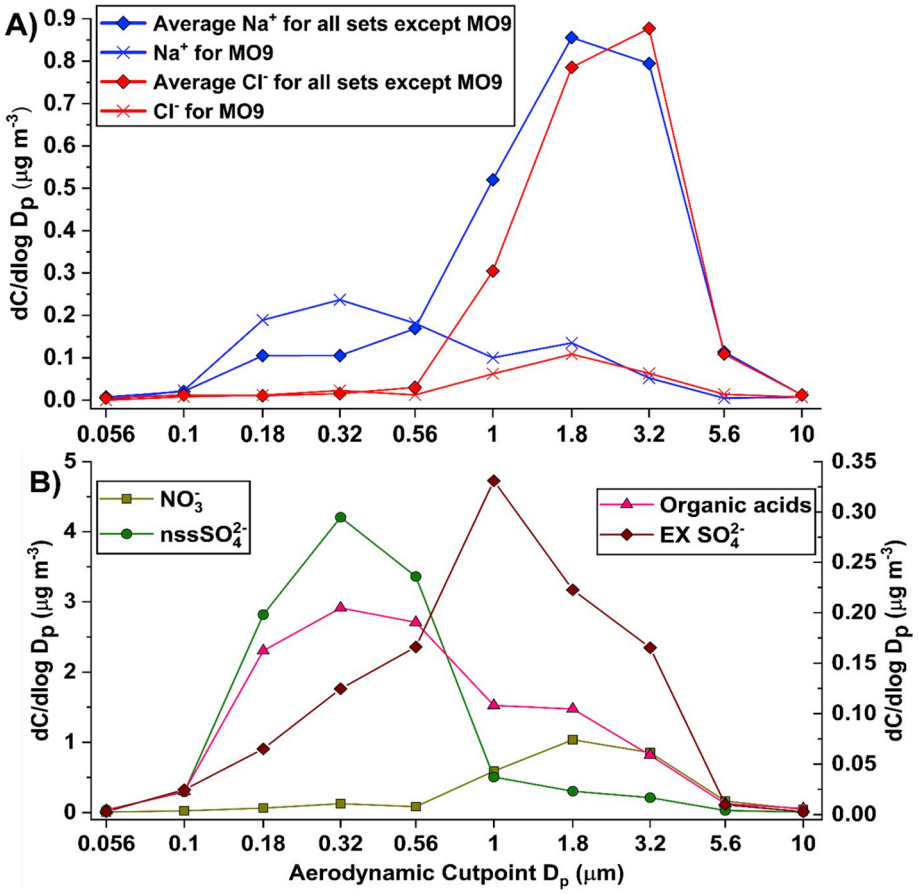

Fig. 5. Mass size distributions of A) total Na^+ and Cl^-, and B) acids participating in Cl^- depletion reactions (nss and ex SO_4^{2-} NO_3^-, organic acids) for all MOUDI sets except set MO9. Set MO9 (presented with cross markers in panel A) exhibits peculiarly different behavior with a more pronounced peak in the submicrometer range for Na^+.

Future work is warranted to examine such temporal differences in Cl^- depletion effects with more organic acid data in conjunction with SO_4^{2-} and NO_3^-.

To expand on the Cl^- depletion results, the MOUDI sets were further categorized into five separate categories based on pollution characteristics, as demonstrated by Braun et al. (Submitted for publication) for the same dataset. Using a combination of aerosol composition data, HYSPLIT back-trajectories, and data from the Navy Aerosol Analysis and Prediction System (NAAPS) (https://www.nrlmry.navy.mil/aerosol/) (Lynch et al., 2016), the categories were defined as follows along with their associated MOUDI sets and total water-soluble mass concentrations (μg m^{-3}): "Clean" = MO11 (2.7); "Highest Rain" = MO9 (6.2); "Fire" = MO7/8 (13.25 ± 0.45); "Continental Pollution" = MO12/14 (15.05 ± 1.55); "Background" = MO1-2/4–6/

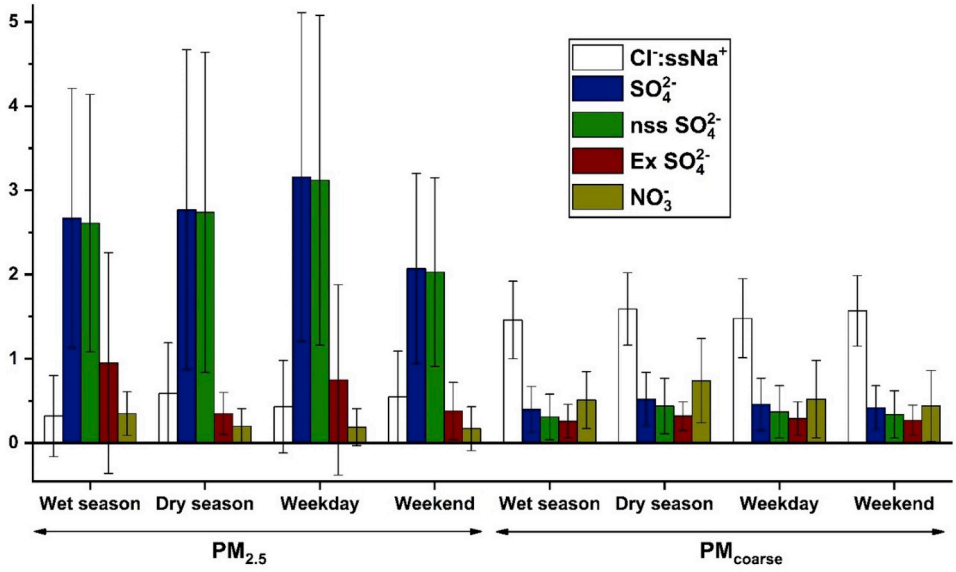

Fig. 6. Comparison of the Cl^-:$ssNa^+$ ratio (unitless) and mass concentrations of different acidic anions (units of $\mu g\ m^{-3}$) for wet and dry seasons and weekend (Saturday and Sunday) and weekdays (Monday-Friday). Data points with Ex $SO_4^{2-} < 0$ are excluded. Numerical values in the figure are summarized in Table S4.

10/15–21 (5.77 ± 1.3). "Clean" represents the MO set with the lowest total water-soluble mass. "Highest Rain" is for the set described already with the unusual mass size distribution of Na^+ that exhibits a more dominant peak in the submicrometer mode. "Fire" includes two sets impacted by transported biomass burning emissions from southwest of Manila close to Borneo and Sumatra, as confirmed by HYSPLIT trajectories, NAAPS results showing the movement of smoke northeast towards to study site, and enhanced levels of the biomass burning marker K ($0.40 \pm 0.01\ \mu g\ m^{-3}$ vs $0.17 \pm 0.05\ \mu g\ m^{-3}$ for the other categories). "Continental Pollution" includes sets impacted by East Asia air masses that have the highest overall water-soluble mass concentrations of sets not impacted by biomass burning. Lastly, "Background" includes all other sets.

Fig. 7 compares the overall composition of the MOUDI sets included in each category along with the mean $\%Cl^-$ depletion. The least (21.3%) and most depletion (90.7%) occurred in the "Clean" and "Highest Rain" categories, respectively. The "Continental Pollution" category exhibited the second highest Cl^- depletion (79.4%) owing to its elevated cumulative amount of acids (i.e., Ex SO_4^{2-}, NO_3^-, organic

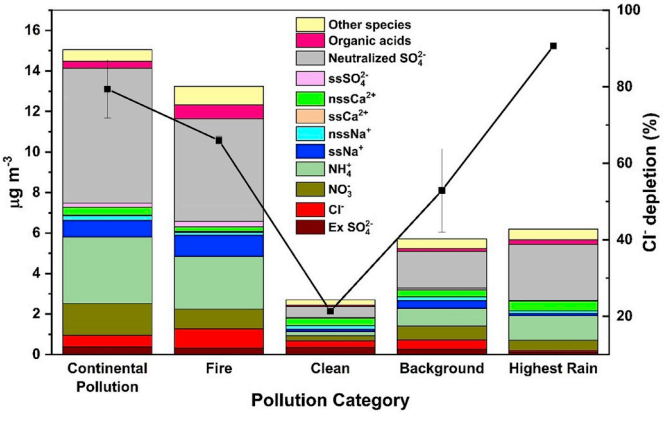

Fig. 7. Water-soluble mass concentrations associated with different species categorized based on the five types of pollution characteristics. On the right y-axis is the $\%Cl^-$ depletion for each category. The 'organic acids' category includes carboxylic acids (Pyruvate, Adipate, Succinate, Maleate, Oxalate, Phthalate) and MSA. 'Other species' includes all the elements analyzed using IC and ICP-QQQ (listed in Section 2.2) that are not shown in this figure.

acids: $2.28\ \mu g\ m^{-3}$). In contrast, the "Clean" category only had $0.68\ \mu g\ m^{-3}$ of those same acids. Worth noting is that all categories except "Highest Rain" ($0.13\ \mu g\ m^{-3}$) exhibited similar amounts of Ex SO_4^{2-} (0.26–$0.38\ \mu g\ m^{-3}$), with the key difference driving the variability in $\%Cl^-$ depletion being the overall amount of NO_3^- (wider range of 0.24–$1.57\ \mu g\ m^{-3}$) that is concentrated in the supermicrometer sizes as compared to the other acids (Fig. 5B). "Fire" sets exhibited higher Cl^- depletion compared to "Background" sets even though both categories had similar Ex SO_4^{2-}. For these five pollution categories, there was more enhanced Cl^- depletion in the submicrometer stages as compared to larger sizes (Fig. 8) coincident with higher concentrations of nssSO_4^{2-} and organic acids (Fig. 5B). More specifically, the ratios of $\%Cl^-$ depletion for submicrometer stages relative to supermicrometer stages were as follows: "Continental Pollution" = 1.58, "Fire" = 2.15, "Background" = 3.26. "Highest Rain" and "Clean" have no ratios owing to zero $ssNa^+$ and zero $\%Cl^-$ depletion in the supermicrometer range, respectively.

For context in relation to a nearby region, Song et al. (2018) examined Cl^- depletion using shipboard total suspended particle (TSP) measurements over the western South China Sea and observed depletion levels of 73 ± 23% and further showed that Ex SO_4^{2-} and oxalate accounted for the majority of depletion in samples impacted by biomass burning. In contrast, Hsu et al. (2007) observed mean Cl^- depletion levels of 90% for $PM_{2.5}$ and reduced levels for PM_{coarse} (30%) over the northern South China Sea. These and numerous other studies have demonstrated that Cl^- depletion is a prevalent phenomenon in marine regions caused by a variety of acids such as SO_4^{2-}, NO_3^-, and organic acids.

Fig. 9 shows the theoretical maximum of Cl^- depletion attributable to inorganic and organic acids (i.e., Equation (9)) for sub- and supermicrometer particles. Organic acids show potential to be important agents in Cl^- depletion for the submicrometer range, especially when accounting for the neutralization of SO_4^{2-} by NH_4^+. NO_3^- could account for the most depletion in the supermicrometer range (up to 86.4%) as expected based on its mass size distribution exhibiting a peak coincident with major sea salt constituents. It also could have a non-negligible impact in the submicrometer range, potentially accounting for 17.6%–54.8% of the Cl^- depletion observed.

Inorganic acids are more commonly linked to Cl^- depletion, but it is important to also consider organic acids. Sulfate and NO_3^- are stronger acids than organic acids and would be favored for depletion reactions as

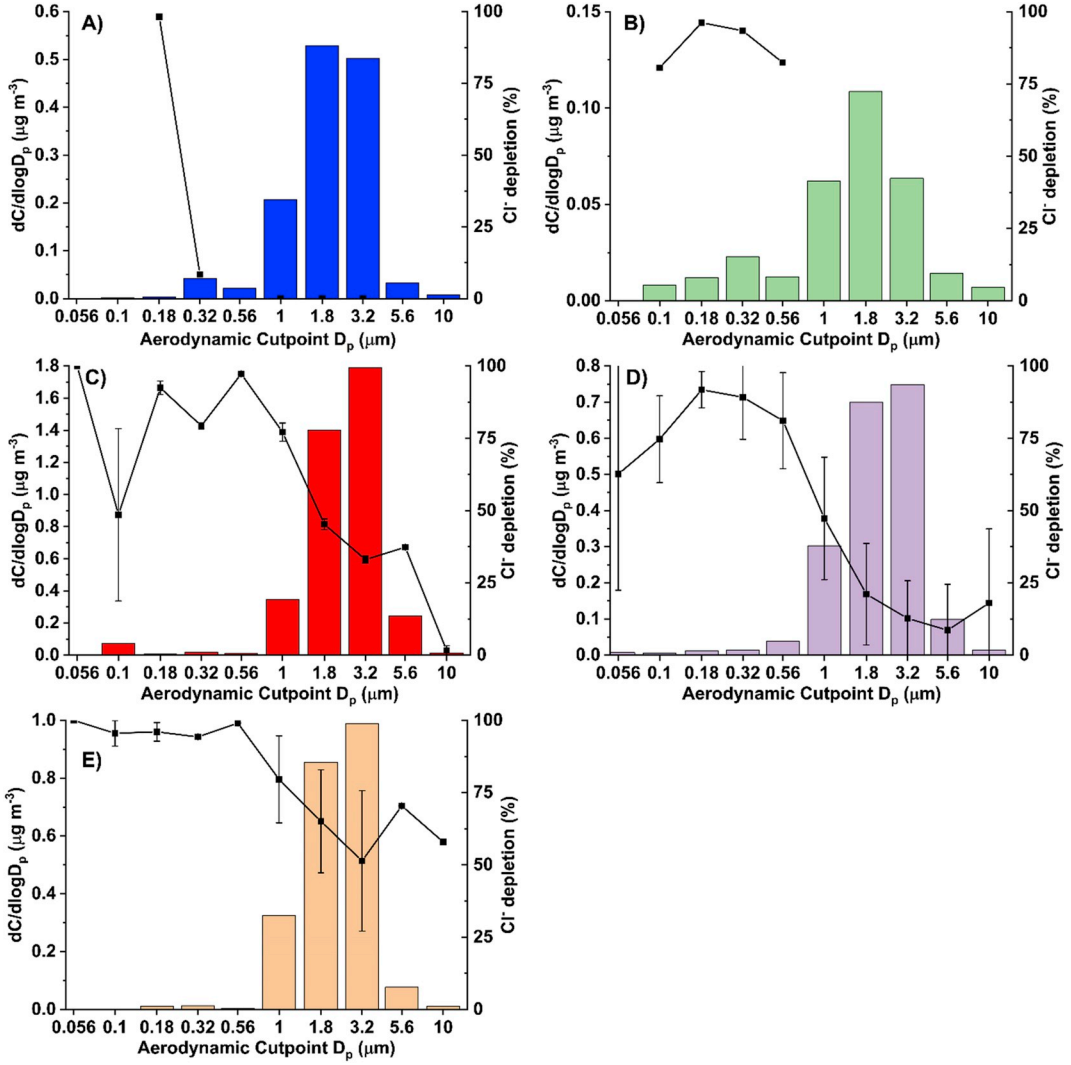

Fig. 8. Average mass size distributions for Cl^- and the %Cl^- depletion for the five different pollutant categories: A) Clean, B) Highest Rain, C) Fire, D) Background and E) Continental Pollution. The bars correspond to left y-axis and lines with markers refer to the right y-axis.

they deprotonate more readily; however, as they cannot always add up to 100% Cl^- depletion, organic acids can participate in such reactions. Oxalate displayed the highest theoretical contribution to Cl^- depletion among the organic acids measured, consistent with it being the most abundant organic acid. Organic acids (especially the longer-chain organic acids of adipate, succinate, and phthalate) reached high theoretical maximum contributions to Cl^- depletion for the "Fire" category. The effect of organic acids is not just limited to the submicrometer range but can also be seen in the supermicrometer range as evidenced by the "Background" category where organic acids could account for up to 40.4% of the observed supermicrometer Cl^- depletion. Regardless of the pollution category, the organic acids can be influential for Cl^- depletion as has been demonstrated recently in other regions such as coastal California (Braun et al., 2017) and the South China Sea (Song et al., 2018).

3.4. Sea salt enrichment factor analysis

As a way to quantify the degree of contamination of sea salt particles, enrichment factors (EF) were quantified for a host of species (Table 2). Analysis of sea salt EF values were conducted using concentrations from MOUDI samples for the three stages with the peak in sea salt mass (1–5.6 μm). EF values > 10 often signify species that have a non-sea salt contribution such as from anthropogenic sources, whereas values ≤ 10 have a significant contribution from sea water (Zhang et al., 2015). As expected, key constituents of sea salt exhibited values below 10 (e.g., Cl^-, Mg^{2+}, K). The various forms of SO_4^{2-} (NSS, Ex, total) exhibited values below 10 with a possible explanation that the source in the three supermicrometer stages of interest could be of marine origin (i.e., dimethylsulfide). Most of the remaining species in Table 2 exhibited very high EF levels (Fe, Al, Ba, Mn, Pb, NO_3^-, V, Zn, NH_4^+). Some of these species are linked to crustal emissions such as dust (Fe, Al, Mn) (Dadashazar et al., 2019; Ma et al., 2019), whereas others (e.g., Pb, V, Zn) are more linked to urban emissions such as combustion, shipping, water processing, and smelting (Nriagu, 1989; Prabhakar et al., 2014). These results indicate that sea salt-containing particles exhibit high levels of contamination in the study region owing to mixing between marine air and other air masses.

3.5. Hygroscopicity analysis

The objective of the hygroscopicity analysis is to determine how κ varies across different stages in relationship with composition, especially with a focus on the relative amount of sea salt. Petters and Kreidenweis (2007) give a κ range of 0.1–0.9 for atmospheric aerosol. Values of 0.1–0.5 are common for a variety of air mass types (marine, urban, biogenic, biomass burning, remote, free tropospheric) in other regions (Chang et al., 2010; Dusek et al., 2010; Hersey et al., 2013;

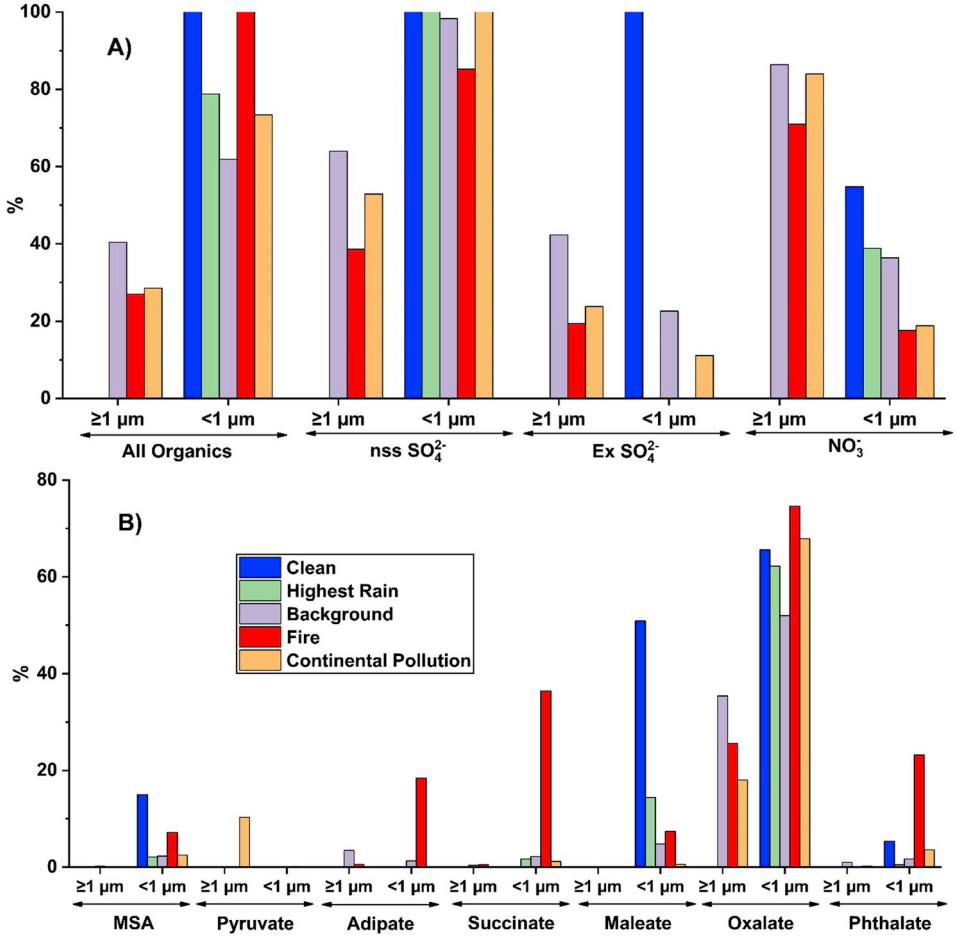

Fig. 9. The percent contribution attributable to different species to Cl^- depletion for different sample set categories based on pollution characteristics. The group "All Organics" in panel A) is categorized into its individual species in panel B). Numerical values in this figure are summarized in Table S5.

Sarangi et al., 2019; Shingler et al., 2016; Shinozuka et al., 2009).

For this study, κ ranged from 0.02 to 0.31 among all the stages from individual sets. The low κ values are not surprising given the polluted nature of Manila with high levels of organics and BC, as shown by the size-resolved profile of volume fractions of different aerosol constituents in Fig. 10A. More specifically, organics and BC cumulatively accounted for 61%–99% of the mass concentration across the 11 MOUDI stages when averaged across all MOUDI sets. Fig. 10B shows the size-resolved profile of κ based on the cumulative average of all MOUDI sets, where a bimodal profile is evident with peaks in κ at

Table 2
Sea salt enrichment factor (ssEF) values calculated using Equation (10). $ssNa^+$ is used as the reference species in the sample and the control. The concentrations used in this analysis represent the sum from the three MOUDI stages (cutpoint D_p = 1, 1.8, 3.2 μm) with the highest sea salt concentrations. MO9 is not shown in the table since the $ssNa^+$ concentrations for all the cutpoints above 1 μm is zero.

	Cl^-	Fe	Ex SO_4^{2-}	Mg^{2+}	nss SO_4^{2-}	SO_4^{2-}	K	Ca^{2+}	Al	Ba	Mn	Pb	NO_3^-	V	Zn	NH_4^+
MO1	0.5	1256	1.5	1.8	2.0	3.1	4.0	8.6	149	1870	4704	9696	18249	27282	44817	92387
MO2	0.7	47	1.5	1.6	1.6	2.9	3.0	13.7	60	2015	3695	3037	26392	41077	29938	29192
MO4	0.6	881	3.5	1.9	4.1	5.4	3.6	16.3	110	3036	6749	3522	27375	40266	81330	119091
MO5	0.4	72	1.3	1.5	2.1	3.2	3.0	5.1	62	1097	3083	916	24064	15998	8570	154792
MO6	1.4	4924	6.9	4.1	8.0	10.8	13.9	85.8	577	4606	15008	8342	85856	61301	122003	239708
MO7	0.6	1342	1.0	1.5	1.6	2.7	1.7	5.6	127	473	1679	1903	14389	3573	4719	111865
MO8	0.5	1933	1.6	1.7	2.3	3.5	2.0	8.6	177	549	2329	1532	16331	4501	6670	140779
MO10	1.6	13139	24.6	8.9	37.2	42.7	26.7	230.7	1150	22795	43859	132581	237420	365657	926482	2584382
MO11	2.3	10605	5.9	5.0	6.6	9.7	8.8	98.4	1225	5134	22851	5686	42635	70841	56864	162590
MO12	0.6	985	1.3	1.6	1.7	2.9	1.2	9.8	83	860	2632	3601	24672	12169	25384	73718
MO14	0.2	2038	3.2	2.0	5.0	6.6	2.7	26.2	188	1832	5303	7768	56248	28575	39404	384972
MO15	3.1	102033	54.2	22.4	120	121	197.1	836.7	5380	87457	367320	655929	1052907	1700556	7435679	9543761
MO16	0.7	7987	4.4	3.0	5.5	6.6	5.2	50.3	441	6770	16160	17758	51725	34529	116536	235036
MO17	0.9	1932	0.5	1.7	1.4	2.4	2.4	17.4	117	2027	4588	4312	15234	13417	49356	179753
MO18	0.8	1663	0.5	1.5	1.3	2.3	2.0	14.1	113	2352	4319	7712	19011	17995	59924	165428
MO19	0.8	2480	1.5	1.8	1.9	3.0	3.0	22.8	202	1828	4724	3515	18361	9842	9596	191928
MO20	0.8	2013	0.8	1.7	1.8	2.8	1.9	19.8	122	2063	6931	2357	24117	18335	35272	397800
MO21	0.9	824	0.2	1.3	0.5	1.4	1.2	7.8	44	703	1541	611	9463	2853	8560	170280

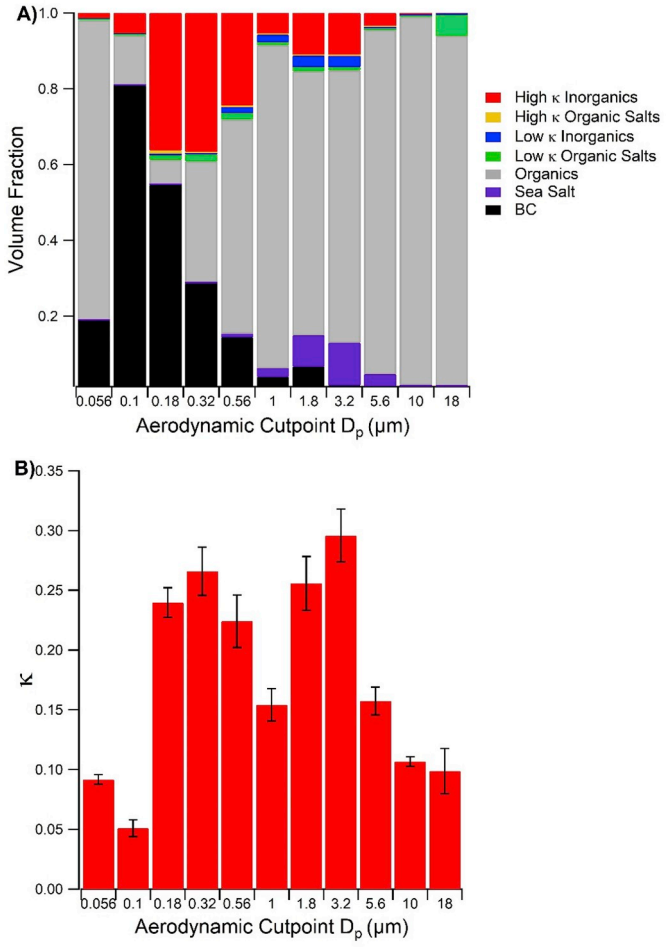

Fig. 10. A) Volume fraction of different aerosol constituents for each MOUDI stage based on the cumulative average of all sets in Table 1. B) Corresponding κ values for each stage as an average of all MOUDI sets, with whiskers representing one standard deviation. The categories in panel A) refer to species defined in Table S2: "Low κ Organic Salts" include CaOxalate, MgOxalate, and ZnOxalate; "High κ Organic Salts" include Na_2Oxalate; "Low κ Inorganics" include $CaSO_4$ and $MgSO_4$; "High κ Inorganics" include $(NH_4)_2SO_4$, K_2SO_4, $Mg(NO_3)_2$, $NaNO_3$, Na_2SO_4, $CaCl_2$, $MgCl_2$, and $Ca(NO_3)_2$; and "Organics" include all organics not contained in the two organic salt categories.

cutpoint diameters of 0.32 μm (0.27) and 3.2 μm (0.30). Expectedly, those two MOUDI stages coincided with the lowest cumulative volume fractions of organics and BC. The 0.32–0.56 μm stage was coincident with the highest volume fraction (0.37) of components categorized as being "high κ Inorganics": $(NH_4)_2SO_4$, K_2SO_4, $Mg(NO_3)_2$, $NaNO_3$, Na_2SO_4, $CaCl_2$, $MgCl_2$, and $Ca(NO_3)_2$. Conversely, the 3.2–5.6 μm stage exhibited the highest volume fraction for sea salt (0.11). Sea salt was also very influential in driving up the value of κ to 0.26 for the 1.8–3.2 μm stage. An important point of this analysis is that the reported values of κ were still much lower than that of pure sea salt (1.24), indicative of the overwhelming influence of other pollution sources mixing with sea salt, especially organics and BC, which were most influential of all aerosol constituents owing to their low assigned κ values and dominant volume fractions across all MOUDI stages. When the analysis in Fig. 10B was repeated for each of the five pollution categories defined in Section 3.3, there was hardly any difference in κ values at fixed sizes (Fig. S3), which again speaks to the dominant contribution from organics and BC to κ.

Future work is warranted to take on a more rigorous approach to calculating κ for the organics in this study region as they represent a dominant fraction of the PM across the spectrum of sizes examined here (Fig. 10A). For this study, all organics (excluding organic salts) were assigned a κ value of 0.1 as a representative value based on past reports (Dusek et al., 2010; Hersey et al., 2013), but the actual κ values for organics can vary from 0.06 to 0.26 depending on the oxygen to carbon ratio as noted in recent work for a variety of air mass types (Li et al., 2019; Shingler et al., 2016).

3.6. Particle morphology

Previous investigations of sea salt aerosol morphology have shown that sea salt particles typically are cubic in nature but with certain attributes such as having "halos" of other species in the case of aged sea salt (Hoffman et al., 2004; Laskin et al., 2002, 2012). Based on EDX evidence of Na^+ and Cl^- enrichment, representative particles containing these elements are shown for three supermicrometer MOUDI stages with aerodynamic cutpoint diameters ranging from 1.8 to 10 μm (Fig. 11). The particles shown in the six images all exhibit non-spherical morphology with Cl^-:Na^+ mass ratios varying from 1.18 to 1.94 with an average of 1.64. The particles in the 1.8–3.2 μm stage have a cubical shape but with rounded edges. The particles in the larger stages exhibited more complex morphologies with rounded edges and evidence of holes and other species attached to the outer peripheries. These Na^+- and Cl^--containing particles all reveal evidence of mixing with other pollutant types and undergoing chemical processing, which is confirmed by Fe, Mo, and Co being present in the various particles based on EDX analysis. The presence of these elements, which have anthropogenic sources in the study region (Cruz et al., 2019), is shown in Fig. S4. Interestingly for the particles shown in Fig. 11B/D/E, O was enriched in areas where Cl^- was not, and vice versa, while Na^+ covered the entire particles. This is in accordance with previous study that discussed the morphology of fresh and aged sea salt in contact with acidic gases (Chi et al., 2015).

4. Conclusions

This study reported on different aerosol datasets in Metro Manila with a focus on sea salt characteristics and their dependence on meteorology and mixing with non-marine air masses. Although sea salt is not the most abundant aerosol type measured in Metro Manila, the results of this study have broad relevance to other marine regions and especially coastal cities owing to the insights this study provides for relationships between precipitation and sea salt, impacts of other air masses mixing with marine aerosols, size-resolved characteristics of aerosol, and chemical reactivity of sea salt as a function of size and different temporal scales. The main results of this work are as follows:

- Sea salt variability, especially the large changes during the wet season, is driven largely by precipitation owing to wet scavenging. The analysis revealed a stronger anti-relationship between sea salt and precipitation accumulation when the latter value was integrated over a larger area encompassing the study site as compared to just from the study site.
- There was significant sea salt chemical reactivity in the study region owing to inorganic and organic acids stemming from a wide variety of sources. Chloride depletion was more pronounced in the wet season as compared to dry periods and during weekdays relative to weekend days.
- Enrichment factor analysis showed that sea salt aerosols were highly contaminated with crustal and anthropogenic pollutants (Fe, Al, Ba, Mn, Pb, NO_3^-, V, Zn, NH_4^+). Morphological results revealed complex

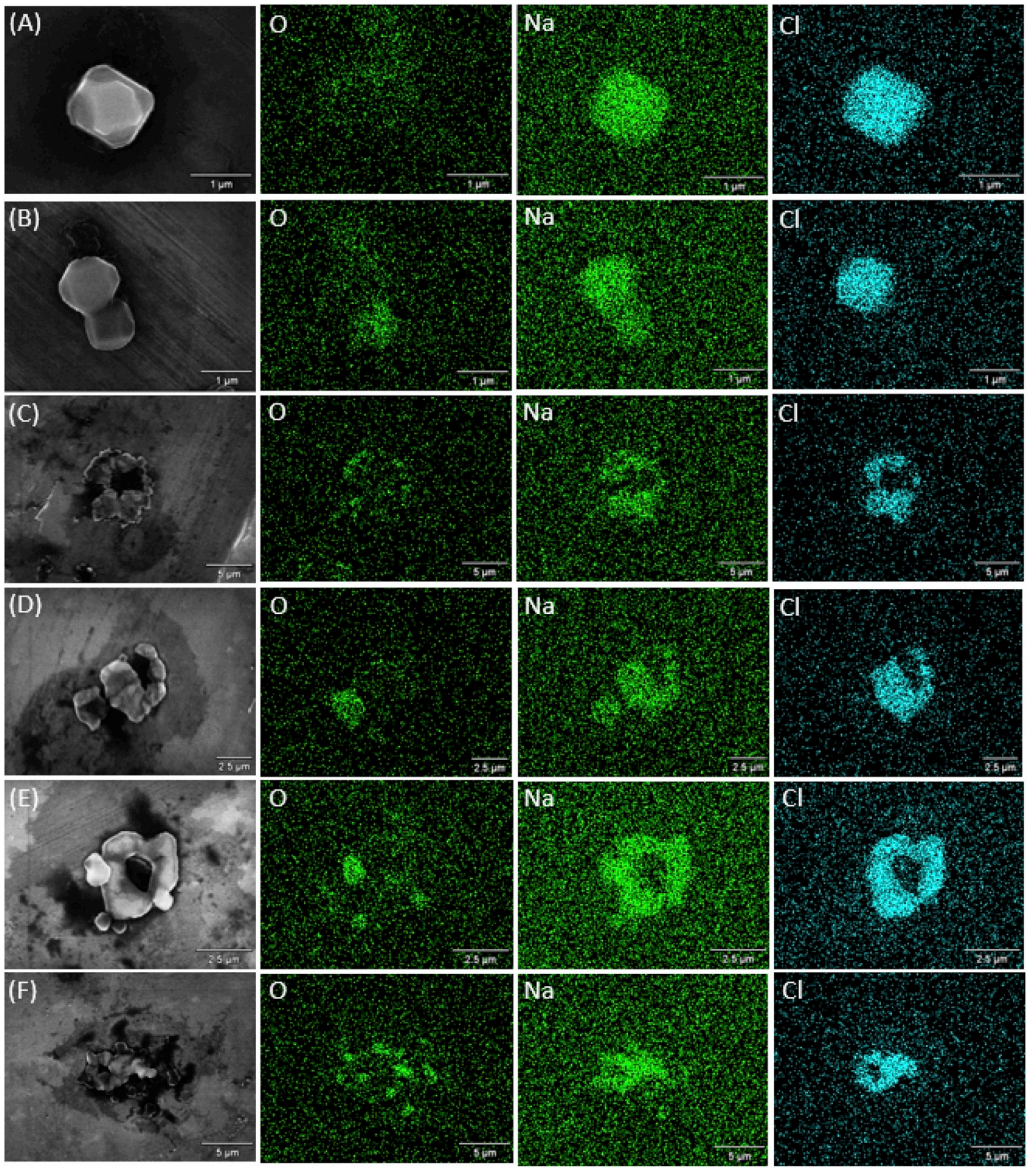

Fig. 11. Size-resolved SEM-EDX characterization of representative particles containing Na and Cl collected at MO on 1 August 2018. The panels correspond to MOUDI stages with the following D_p ranges: (A/B) 1.8–3.2 μm; (C/D) 3.2–5.6 μm; (E/F) 5.6–10 μm. Also shown for each substrate sample are O, Na, and Cl distributions in the individual particles based on EDX analysis.

non-spherical shapes for sea salt-containing particles owing to mixing of sea salt with other pollutants.

- Values of the hygroscopicity parameter, κ, ranged from 0.02 to 0.31 with a bimodal profile across all MOUDI stages. Low values coincided with higher enrichment of BC and water-insoluble organic species in contrast with the highest values being in the stages most enriched with either high-κ inorganic species (0.32–0.56 μm) or sea salt (3.2–5.6 μm). Values are considerably lower than pure sea salt owing to the overwhelming influence of other air masses mixing with sea salt.

Declaration of competing interest

The authors declare that they have no known competing financial interests or personal relationships that could have appeared to influence the work reported in this paper.

Acknowledgements

This research was funded by NASA grant 80NSSC18K0148. We acknowledge Agilent Technologies for their support and Shane Snyder's laboratories for ICP-MS data. We acknowledge the Swedish International Development Cooperation Agency (Sida) for support of the Asian Regional Research Programme on Environmental Technology (ARRPET) project that allowed for the data used between August 2005–October 2007. A. MacDonald acknowledges support from the Mexican National Council for Science and Technology (CONACYT). R. A. Braun acknowledges support from the ARCS Foundation.

Appendix A. Supplementary data

Supplementary data to this article can be found online at https://doi.org/10.1016/j.atmosenv.2019.116922.

References

Artaxo, P., Gerab, F., Yamasoe, M.A., Martins, J.V., 1994. Fine mode aerosol composition at 3 long-term atmospheric monitoring sites in the Amazon basin. J. Geophys. Res. Atmos. 99, 22857–22868. https://doi.org/10.1029/94jd01023.

Bagtasa, G., Cayetano, M.G., Yuan, C.S., 2018. Seasonal variation and chemical characterization of PM2.5 in northwestern Philippines. Atmos. Chem. Phys. 18, 4965–4980. https://doi.org/10.5194/acp-18-4965-2018.

Becagli, S., Proposito, M., Benassai, S., Gragnani, R., Magand, O., Traversi, R., Udisti, R., 2005. Spatial distribution of biogenic sulphur compounds (MSA, nssSO(4)(2-)) in the northern Victoria Land-Dome C-Wilkes Land, area, East Antarctica. Ann. Glaciol. 41, 23–31. https://doi.org/10.3189/172756405781813384.

Bellouin, N., Quaas, J., Morcrette, J.J., Boucher, O., 2013. Estimates of aerosol radiative forcing from the MACC re-analysis. Atmos. Chem. Phys. 13, 2045–2062. https://doi.org/10.5194/acp-13-2045-2013.

Boreddy, S.K.R., Kawamura, K., 2015. A 12-year observation of water-soluble ions in TSP aerosols collected at a remote marine location in the western North Pacific: an outflow region of Asian dust. Atmos. Chem. Phys. 15, 6437–6453 10.5194/acp-15-6437-2015.

Bowen, H.J.M., 1979. Environmental Chemistry of the Elements. Academic Press, London.

Braun, R.A., AzadiAghdam, M., Bañaga, P.A., Betito, G., Cambaliza, M.O., Cruz, M.T., Lorenzo, M.R., MacDonald, A.B., Simpas, J.B., Stahl, C., Sorooshian, A., Submitted for publication. Long-range transport mechanisms in east and southeast Asia and impacts on size-resolved aerosol composition: contrasting high and low aerosol loading events. Atmos. Chem. Phys. Discuss.,.

Braun, R.A., Dadashazar, H., MacDonald, A.B., Aldhaif, A.M., Maudlin, L.C., Crosbie, E., Aghdam, M.A., Mardi, A.H., Sorooshian, A., 2017. Impact of wildfire emissions on chloride and bromide depletion in marine aerosol particles. Environ. Sci. Technol. 51 (16), 9013–9021. https://doi.org/10.1021/acs.est.7b02039.

Chameides, W.L., Stelson, A.W., 1992. Aqueous-phase chemical processes in deliquescent sea-salt aerosols - a mechanism that couples the atmospheric cycles of S and sea salt. J. Geophys. Res. Atmos. 97, 20565–20580. https://doi.org/10.1029/92jd01923.

Chang, R.Y.W., Slowik, J.G., Shantz, N.C., Vlasenko, A., Liggio, J., Sjostedt, S.J., Leaitch, W.R., Abbatt, J.P.D., 2010. The hygroscopicity parameter (kappa) of ambient organic aerosol at a field site subject to biogenic and anthropogenic influences: relationship to degree of aerosol oxidation. Atmos. Chem. Phys. 10, 5047–5064. https://doi.org/10.5194/acp-10-5047-2010.

Chi, J.W., Li, W.J., Zhang, D.Z., Zhang, J.C., Lin, Y.T., Shen, X.J., Sun, J.Y., Chen, J.M., Zhang, X.Y., Zhang, Y.M., Wang, W.X., 2015. Sea salt aerosols as a reactive surface for inorganic and organic acidic gases in the Arctic troposphere. Atmos. Chem. Phys. 15, 11341–11353. https://doi.org/10.5194/acp-15-11341-2015.

China, S., Burrows, S.M., Wang, B., Harder, T.H., Weis, J., Tanarhte, M., Rizzo, L.V., Brito, J., Cirino, G.G., Ma, P.-L., Cliff, J., Artaxo, P., Gilles, M.K., Laskin, A., 2018. Fungal spores as a source of sodium salt particles in the Amazon basin. Nat. Commun. 9, 4793. https://doi.org/10.1038/s41467-018-07066-4.

Cohen, D.D., Stelcer, E., Santos, F.L., Prior, M., Thompson, C., Pabroa, P.C.B., 2009. Fingerprinting and source apportionment of fine particle pollution in Manila by IBA and PMF techniques: a 7-year study. X Ray Spectrom. 38, 18–25. https://doi.org/10.1002/xrs.1112.

Cruz, F.T., Narisma, G.T., Villafuerte, M.Q., Chua, K.U.C., Olaguera, L.M., 2013. A climatological analysis of the southwest monsoon rainfall in the Philippines. Atmos. Res. 122, 609–616. https://doi.org/10.1016/j.atmosres.2012.06.010.

Cruz, M.T., Bañaga, P.A., Betito, G., Braun, R.A., Stahl, C., Aghdam, M.A., Cambaliza, M.O., Dadashazar, H., Hilario, M.R., Lorenzo, G.R., Ma, L., MacDonald, A.B., Pabroa, P.C., Yee, J.R., Simpas, J.B., Sorooshian, A., 2019. Size-resolved composition and morphology of particulate matter during the Southwest Monsoon in Metro Manila, Philippines. Atmos. Chem. Phys (in press). https://doi.org/10.5194/acp-2019-270.

Dadashazar, H., Ma, L., Sorooshian, A., 2019. Sources of pollution and interrelationships between aerosol and precipitation chemistry at a central California site. Sci. Total Environ. 651, 1776–1787. https://doi.org/10.1016/j.scitotenv.2018.10.086.

Dusek, U., Frank, G.P., Curtius, J., Drewnick, F., Schneider, J., Kurten, A., Rose, D., Andreae, M.O., Borrmann, S., Poschl, U., 2010. Enhanced organic mass fraction and decreased hygroscopicity of cloud condensation nuclei (CCN) during new particle formation events. Geophys. Res. Lett. 37. https://doi.org/10.1029/2009GL040930.

Farren, N.J., Dunmore, R.E., Mead, M.I., Nadzir, M.S.M., Abu Samah, A., Phang, S.M., Bandy, B.J., Sturges, W.T., Hamilton, J.F., 2019. Chemical characterisation of water-soluble ions in atmospheric particulate matter on the east coast of Peninsular Malaysia. Atmos. Chem. Phys. 19, 1537–1553. https://doi.org/10.5194/acp-19-1537-2019.

Gysel, M., Crosier, J., Topping, D.O., Whitehead, J.D., Bower, K.N., Cubison, M.J., Williams, P.I., Flynn, M.J., McFiggans, G.B., Coe, H., 2007. Closure study between chemical composition and hygroscopic growth of aerosol particles during TORCH2. Atmos. Chem. Phys. 7, 6131–6144. https://doi.org/10.5194/acp-7-6131-2007.

Hersey, S.P., Craven, J.S., Metcalf, A.R., Lin, J., Lathem, T., Suski, K.J., Cahill, J.F., Duong, H.T., Sorooshian, A., Jonsson, H.H., Shiraiwa, M., Zuend, A., Nenes, A., Prather, K.A., Flagan, R.C., Seinfeld, J.H., 2013. Composition and hygroscopicity of the Los Angeles aerosol: CalNex. J. Geophys. Res. Atmos. 118, 3016–3036. https://doi.org/10.1002/jgrd.50307.

Hoffman, R.C., Laskin, A., Finlayson-Pitts, B.J., 2004. Sodium nitrate particles: physical and chemical properties during hydration and dehydration, and implications for aged sea salt aerosols. J. Aerosol Sci. 35, 869–887. https://doi.org/10.1016/j.jaerosci.2004.02.003.

Hong, Y., Hsu, K.L., Sorooshian, S., Gao, X.G., 2004. Precipitation estimation from remotely sensed imagery using an artificial neural network cloud classification system. J. Appl. Meteorol. 43, 1834–1852. https://doi.org/10.1175/Jam2173.1.

Hsu, S.-C., Liu, S.C., Kao, S.-J., Jeng, W.-L., Huang, Y.-T., Tseng, C.-M., Tsai, F., Tu, J.-Y., Yang, Y., 2007. Water-soluble species in the marine aerosol from the northern South China Sea: high chloride depletion related to air pollution. J. Geophys. Res.: Atmosphere 112. https://doi.org/10.1029/2007jd008844.

Hudson, P.K., Murphy, D.M., Cziczo, D.J., Thomson, D.S., de Gouw, J.A., Warneke, C., Holloway, J., Jost, H.-J., Hübler, G., 2004. Biomass-burning particle measurements: characteristic composition and chemical processing. J. Geophys. Res. 109. https://doi.org/10.1029/2003jd004398.

Kerminen, V.M., Teinila, K., Hillamo, R., Pakkanen, T., 1998. Substitution of chloride in sea-salt particles by inorganic and organic anions. J. Aerosol Sci. 29, 929–942. https://doi.org/10.1016/S0021-8502(98)00002-0.

Laskin, A., Iedema, M.J., Cowin, J.P., 2002. Quantitative time-resolved monitoring of nitrate formation in sea salt particles using a CCSEM/EDX single particle analysis. Environ. Sci. Technol. 36, 4948–4955. https://doi.org/10.1021/es020551k.

Laskin, A., Moffet, R.C., Gilles, M.K., Fast, J.D., Zaveri, R.A., Wang, B., Nigge, P., Shutthanandan, J., 2012. Tropospheric chemistry of internally mixed sea salt and organic particles: surprising reactivity of NaCl with weak organic acids. J. Geophys. Res.: Atmosphere 117. https://doi.org/10.1029/2012jd017743.

Lee, Y.-N., Weber, R., Ma, Y., Orsini, D., Maxwell-Meier, K., Blake, D., Meinardi, S., Sachse, G., Harward, C., Chen, T.-Y., Thornton, D., Tu, F.-H., Bandy, A., 2003. Airborne measurement of inorganic ionic components of fine aerosol particles using the particle-into-liquid sampler coupled to ion chromatography technique during ACE-Asia and TRACE-P. J. Geophys. Res.: Atmosphere 108. https://doi.org/10.1029/2002jd003265.

Lewis, E., Schwartz, S., 2004. sea salt aerosol production: mechanisms, methods, measurements, and models—a critical review. https://doi.org/10.1029/GM152.

Li, X., Song, S., Zhou, W., Hao, J., Worsnop, D.R., Jiang, J., 2019. Interactions between aerosol organic components and liquid water content during haze episodes in Beijing. Atmos. Chem. Phys. Discuss in review. https://doi.org/10.5194/acp-2019-316.

Liao, H., Chen, W.-T., Seinfeld, J.H., 2006. Role of climate change in global predictions of future tropospheric ozone and aerosols. J. Geophys. Res.: Atmosphere 111. https://doi.org/10.1029/2005jd006852.

Lynch, P., Reid, J.S., Westphal, D.L., Zhang, J.L., Hogan, T.F., Hyer, E.J., Curtis, C.A., Hegg, D.A., Shi, Y.X., Campbell, J.R., Rubin, J.I., Sessions, W.R., Turk, F.J., Walker, A.L., 2016. An 11-year global gridded aerosol optical thickness reanalysis (v1.0) for atmospheric and climate sciences. Geosci. Model Dev. (GMD) 9, 1489–1522. https://doi.org/10.5194/gmd-9-1489-2016.

Ma, L., Dadashazar, H., Braun, R.A., MacDonald, A.B., Aghdam, M.A., Maudlin, L.C., Sorooshian, A., 2019. Size-resolved characteristics of water-soluble particulate elements in a coastal area: source identification, influence of wildfires, and diurnal variability. Atmos. Environ. 206, 72–84. https://doi.org/10.1016/j.atmosenv.2019.02.045.

MacDonald, A.B., Dadashazar, H., Chuang, P.Y., Crosbie, E., Wang, H.L., Wang, Z., Jonsson, H.H., Flagan, R.C., Seinfeld, J.H., Sorooshian, A., 2018. Characteristic vertical profiles of cloud water composition in marine stratocumulus clouds and relationships with precipitation. J. Geophys. Res. Atmos. 123, 3704–3723. https://doi.org/10.1002/2017jd027900.

Marple, V., Olson, B., Romay, F., Hudak, G., Geerts, S.M., Lundgren, D., 2014. Second generation micro-orifice Uniform Deposit impactor, 120 MOUDI-II: design, evaluation, and application to long-term ambient sampling. Aerosol Sci. Technol. 48, 427–433. https://doi.org/10.1080/02786826.2014.884274.

Martens, C.S., Wesolowski, J.J., Harriss, R.C., Kaifer, R., 1973. Chlorine loss from puerto-rican and San-Francisco-bay area marine aerosols. J. Geophys. Res. 78, 8778–8792. https://doi.org/10.1029/JC078i036p08778.

Maudlin, L.C., Wang, Z., Jonsson, H.H., Sorooshian, A., 2015. Impact of wildfires on size-resolved aerosol composition at a coastal California site. Atmos. Environ. 119, 59–68. https://doi.org/10.1016/j.atmosenv.2015.08.039.

McInnes, L.M., Covert, D.S., Quinn, P.K., Germani, M.S., 1994. Measurements of chloride depletion and sulfur enrichment in individual sea-salt particles collected from the remote marine boundary-layer. J. Geophys. Res. Atmos. 99, 8257–8268. https://doi.org/10.1029/93jd03453.

Miller, J.N., Miller, J.C., 2000. Statistics and Chemometrics for Analytical Chemistry. Prentice Hall.

Murphy, D.M., Froyd, K.D., Bian, H.S., Brock, C.A., Dibb, J.E., DiGangi, J.P., Diskin, G., Dollner, M., Kupc, A., Scheuer, E.M., Schill, G.P., Weinzierf, B., Williamson, C.J., Yu, P.F., 2019. The distribution of sea-salt aerosol in the global troposphere. Atmos. Chem. Phys. 19, 4093–4104. https://doi.org/10.5194/acp-19-4093-2019.

Nguyen, P., Sellars, S., Thorstensen, A., Tao, Y.M., Ashouri, H., Braithwaite, D., Hsu, K.L., Sorooshian, S., 2014. Satellites Track Precipitation of Super Typhoon Haiyan. pp. 133–135. Eos. https://doi.org/10.1002/2014EO160002.

Nguyen, P., Shearer, E.J., Tran, H., Ombadi, M., Hayatbini, N., Palacios, T., Huynh, P., Braithwaite, D., Updegraff, G., Hsu, K., Kuligowski, B., Logan, W.S., Sorooshian, S., 2019. The CHRS Data Portal, an easily accessible public repository for PERSIANN global satellite precipitation data. Sci. Data 6, 180296. https://doi.org/10.1038/sdata.2018.296.

Nriagu, J.O., 1989. A global assessment of natural sources of atmospheric trace-metals. Nature 338, 47–49. https://doi.org/10.1038/338047a0.

Petters, M.D., Kreidenweis, S.M., 2007. A single parameter representation of hygroscopic growth and cloud condensation nucleus activity. Atmos. Chem. Phys. 7, 1961–1971. https://doi.org/10.5194/acp-7-1961-2007.

Philippine Statistics Authority, 2015. https://psa.gov.ph/content/2015-psa-annual-report, Accessed date: 2 April 2019.

Prabhakar, G., Sorooshian, A., Toffol, E., Arellano, A.F., Betterton, E.A., 2014. Spatiotemporal distribution of airborne particulate metals and metalloids in a populated arid region. Atmos. Environ. 92, 339–347. https://doi.org/10.1016/j.

atmosenv.2014.04.044.
Quinn, P.K., Bates, T.S., Coffman, D.J., Miller, T.L., Johnson, J.E., Covert, D.S., Putaud, J.P., Neususs, C., Novakov, T., 2000. A comparison of aerosol chemical and optical properties from the 1st and 2nd Aerosol Characterization Experiments. Tellus B 52, 239–257. https://doi.org/10.1034/j.1600-0889.2000.00033.x.
Rolph, G., Stein, A., Stunder, B., 2017. Real-time environmental applications and display system: ready. Environ. Model. Softw 95, 210–228. https://doi.org/10.1016/j.envsoft.2017.06.025.
Sarangi, B., Ramachandran, S., Rajesh, T.A., Dhaker, V.K., 2019. Black carbon linked aerosol hygroscopic growth: size and mixing state are crucial. Atmos. Environ. 200, 110–118. https://doi.org/10.1016/j.atmosenv.2018.12.001.
Seinfeld, J.H., Pandis, S.N., 2006. Atmospheric Chemistry and Physics : from Air Pollution to Climate Change, second ed. Wiley, New York.
Shingler, T., Crosbie, E., Ortega, A., Shiraiwa, M., Zuend, A., Beyersdorf, A., Ziemba, L., Anderson, B., Thornhill, L., Perring, A.E., Schwarz, J.P., Campazano-Jost, P., Day, D.A., Jimenez, J.L., Hair, J.W., Mikoviny, T., Wisthaler, A., Sorooshian, A., 2016. Airborne characterization of subsaturated aerosol hygroscopicity and dry refractive index from the surface to 6.5km during the SEAC(4)RS campaign. J. Geophys. Res. Atmos. 121, 4188–4210. https://doi.org/10.1002/2015jd024498.
Shinozuka, Y., Clarke, A.D., DeCarlo, P.F., Jimenez, J.L., Dunlea, E.J., Roberts, G.C., Tomlinson, J.M., Collins, D.R., Howell, S.G., Kapustin, V.N., McNaughton, C.S., Zhou, J., 2009. Aerosol optical properties relevant to regional remote sensing of CCN activity and links to their organic mass fraction: airborne observations over Central Mexico and the US West Coast during MILAGRO/INTEX-B. Atmos. Chem. Phys. 9, 6727–6742. https://doi.org/10.5194/acp-9-6727-2009.
Silva, P.J., Liu, D.Y., Noble, C.A., Prather, K.A., 1999. Size and chemical characterization of individual particles resulting from biomass burning of local Southern California species. Environ. Sci. Technol. 33, 3068–3076. https://doi.org/10.1021/es980544p.
Song, J.W., Zhao, Y., Zhang, Y.Y., Fu, P.Q., Zheng, L.S., Yuan, Q., Wang, S., Huang, X.F., Xu, W.H., Cao, Z.X., Gromov, S., Lai, S.C., 2018. Influence of biomass burning on atmospheric aerosols over the western South China Sea: insights from ions, carbonaceous fractions and stable carbon isotope ratios. Environ. Pollut. 242, 1800–1809. https://doi.org/10.1016/j.envpol.2018.07.088.
Sorooshian, A., Wonaschütz, A., Jarjour, E.G., Hashimoto, B.I., Schichtel, B.A., Betterton, E.A., 2011. An aerosol climatology for a rapidly growing arid region (southern Arizona): major aerosol species and remotely sensed aerosol properties. J. Geophys. Res. 116. https://doi.org/10.1029/2011jd016197.
Sorooshian, A., Wang, Z., Coggon, M.M., Jonsson, H.H., Ervens, B., 2013. Observations of sharp oxalate reductions in stratocumulus clouds at variable altitudes: organic acid and metal measurements during the 2011 E-PEACE campaign. Environ. Sci. Technol. 47, 7747–7756. https://doi.org/10.1021/es4012383.
Sorooshian, A., Crosbie, E., Maudlin, L.C., Youn, J.S., Wang, Z., Shingler, T., Ortega, A.M., Hersey, S., Woods, R.K., 2015. Surface and airborne measurements of organosulfur and methanesulfonate over the western United States and coastal areas. J. Geophys. Res. Atmos. 120, 8535–8548. https://doi.org/10.1002/2015jd023822.
Stein, A.F., Draxler, R.R., Rolph, G.D., Stunder, B.J.B., Cohen, M.D., Ngan, F., 2015. Noaa's hysplit atmospheric transport and dispersion modeling system. Bull. Am. Meteorol. Soc. 96, 2059–2077. https://doi.org/10.1175/Bams-D-14-00110.1.
Stokes, R.H., Robinson, R.A., 1966. Interactions in aqueous nonelectrolyte solutions .I. Solute-solvent equilibria. J Phys Chem. U.S. 70, 2126. https://doi.org/10.1021/j100879a010.
van Pinxteren, M., Fiedler, B., van Pinxteren, D., Iinuma, Y., Kortzinger, A., Herrmann, H., 2015. Chemical characterization of sub-micrometer aerosol particles in the tropical Atlantic Ocean: marine and biomass burning influences. J. Atmos. Chem. 72, 105–125. https://doi.org/10.1007/s10874-015-9307-3.
Wonaschutz, A., Hersey, S.P., Sorooshian, A., Craven, J.S., Metcalf, A.R., Flagan, R.C., Seinfeld, J.H., 2011. Impact of a large wildfire on water-soluble organic aerosol in a major urban area: the 2009 Station Fire in Los Angeles County. Atmos. Chem. Phys. 11, 8257–8270. https://doi.org/10.5194/acp-11-8257-2011.
Ye, B., Ji, X., Yang, H., Yao, X., Chan, C.K., Cadle, S.H., Chan, T., Mulawa, P.A., 2003. Concentration and chemical composition of PM2.5 in Shanghai for a 1-year period. Atmos. Environ. 37, 499–510. https://doi.org/10.1016/S1352-2310(02)00918-4.
Zdanovskii, A.B., 1948. Novyi metod rascheta rastvorimostei elektrolitov V mnogokomponentnykh sistemakh .2. Zh Fiz Khim+ 22, 1486–1495.
Zhang, Y., Zhang, H.H., Yang, G.P., Liu, Q.L., 2015. Chemical characteristics and source analysis of aerosol composition over the bohai Sea and the Yellow sea in spring and autumn. J. Atmos. Sci. 72, 3563–3573. https://doi.org/10.1175/Jas-D-14-0372.1.
Zhao, Y.L., Gao, Y., 2008. Acidic species and chloride depletion in coarse aerosol particles in the US east coast. Sci. Total Environ. 407, 541–547. https://doi.org/10.1016/j.scitotenv.2008.09.002.